ISSN: 2476- 2334

Research Article

International Journal of Nanotechnology and Nanomedicine

Crystallization, mechanical and electrochemical behavior of Al-Ce-TM (TM = Fe, Co, Ni and Cu) amorphous alloys

Jianqi Zhang[1]*, Chenyuan Chang[1], August Chang[2], Tian Zhao[3], Jiyu Jia[1], Na Na[1], Pengzhong Shi[1], Wenwen Li[1], Shumei Li[4], Qiang Wang[1], Furen You[1], Dianchen Feng[1], Xuemei Wang[1], Yinfeng Zhao[1], Tao Li[1], Yiquan Song[1], Yongchang Huang[5] and Shengli An[1]

[1]*School of Materials & Metallurgy, Inner Mongolia University of Science and Technology, Baotou 014010, P. R. China*

[2]*School of Letters & Science, University of Wisconsin-Madison, Madison, Wisconsin 53706, USA*

[3]*Deep Earth Detection Center, Chinese Academy of Geological Sciences, Beijing 100037, P. R. China*

[4]*Metering and Testing Center, Inner Mongolia First Machinery Group Ltd, Baotou 014030, P. R. China*

[5]*School of Materials Science & Engineering, Shanghai Jiao tong University, Shanghai 200240, P. R. China*

***Corresponding author**

Jianqi Zhang, School of Materials & Metallurgy, Inner Mongolia University of Science and Technology, Baotou 014010, P. R. China; Email: jzhang82@imust.cn

Submitted: 29 Oct 2019; **Accepted:** 08 Nov 2019; **Published:** 15 Nov 2019

Abstract

$Al_{86}Ce_{10}TM_4$ amorphous alloys (TM=Fe, Co, Ni and Cu) were fabricated using melt-spin fast-quenching method. The crystallization, mechanical and electrochemical behavior of the as-spun and the post-annealed alloys were investigated by X-ray diffraction (XRD), differential scanning calorimetry (DSC), micro-indentation and electrochemical techniques. It was found the completely amorphous $Al_{86}Ce_{10}TM_4$ alloys (TM=Fe, Co, Ni and Cu) go through two crystallization processes, where the first exothermal peak represents nucleation of nano-crystalline particles and the second exothermal peak signifies growth of the nano-crystalline precipitates. Both the nucleation and growth processes rely on diffusion-controlled mechanism. The first onset crystallization temperature T_{x1} associated with activation energy E_1 and frequency factor K_{o1} can be used to evaluate the thermal stability of the amorphous alloys while the second onset crystallization temperature T_{x2} associated with activation energy E_2 and frequency factor K_{o2} can be taken to judge the thermal stability of ideal amorphous-nanocrystalline mixed structure in sustaining optimized mechanical and electrochemical properties. The as-spun and post-annealed alloys exhibit higher mechanical hardness (860~1180 MPa), corrosion resistance ($10^{-8}A/cm^2$) and high temperature endurance (284, 300 and 420°C for $Al_{86}Ce_{10}Co_4$, $Al_{86}Ce_{10}Ni_4$ and $Al_{86}Ce_{10}Fe_4$, respectively) compared to hardness 500~600 MPa, corrosion resistance $10^{-7}A/cm^2$ and high temperature durability 200°C of traditional Al crystalline alloys, manifesting the value on scientific studies and engineering applications of the $Al_{86}Ce_{10}TM_4$ amorphous alloys.

Keywords: Amorphous alloys, Al-Ce-TM, Crystallization process, Mechanical hardness, Corrosion resistance

Introduction

Al-based metallic glasses has aroused great interest on the merit of their high mechanical strength and corrosion resistance comparing with the conventional Al crystalline alloys, in particular after Poon and Inoue reported the Al-based amorphous alloys with high tensile strength and good ductility in 1988, investigations on glass formation, thermal stability, crystallization, microstructure and property of the alloys have become the major topics thus far [1-16]. Al-rare earth-transition metal (Al-RE-TM) amorphous alloys known as marginal glass formers that show limited glass-forming ability are particularly of interest. Quite a lot of research regarding glass-forming ability, thermal stability, and crystallization has been reported [17-24]. However, there have been few reports regarding systematic study pinpointing to the effect of transition metals on the Al-RE-TM amorphous alloys. Besides, lots of ambiguity still exists in what crystallization processes evolve and how structures transform throughout crystallization processes. Therefore, there highly needs to investigate how amorphous structure evolves with crystallization processes, and how mechanical and electrochemical behavior performs accompanying with the crystallization evolution.

It is therefore, based on our previous work, we further investigate in this paper the crystallization processes through which what mechanisms stand by, what microstructures proceed, and how mechanical and electrochemical perform regarding $Al_{86}Ce_{10}TM_4$ amorphous alloys (TM=Fe, Co, Ni and Cu) [25].

Experimental

Amorphous $Al_{86}Ce_{10}TM_4$ (TM= Fe, Co, Ni and Cu) ribbons were fabricated by melt-spin fast-quenching method [26]. Pure metals, Al (99.98 wt. %), Ce (99.7 wt. %), Fe (99.7 wt. %), Co (99.7 wt. %), Ni (99.7 wt. %) and Cu (99.7 wt. %) were used as raw materials. Metallic glasses in the final composition of $Al_{86}Ce_{10}TM_4$ (TM=Fe, Co, Ni and Cu) were manufactured after the mixed metals had been melted by induction-heating at high vacuum back-filled with high-purity argon at pressure of 0.04 MPa, remelted and homogenized four times and finally ejection-cast onto a rotating copper roller at a circumferential speed approximately 40 m/s under high-purity helium environment. All the as-spun ribbons were 40 μm in thickness and 4 mm in width. The morphology, composition and structure were examined by transmission electron microscope (TEM, JEM-2100F), scanning electron microscope and energy dispersive spectroscopy (SEM-EDS, QUANTA 400), and X-ray diffraction (XRD, Philips PW1700 using Cu Kα radiation λ=0.1542 nm).

Thermal analysis of the as-spun ribbons was carried out using a Perkins-Elmer DSC-8500 differential scanning calorimeter (DSC) under flowing high-purity argon. To eliminate the random and systematic errors, DSC was calibrated using high-purity In and Zn as standard samples, which provide a temperature accuracy of 0.1 K with an average standard error of 1 K in the measured values. The glass transition and crystallization process were studied by heating the samples from room temperature to 1200 K at heating rates of 20, 40, 80 and 200 K/min. The crystallization kinetics, especially crystallization activation energy, pre-exponential coefficient of effective overall reaction rate, reaction order and types of crystal growth, were evaluated using Kissinger equation and Johnson-Mehl-Avrami (JMA) method [27-32].

To investigate how the fully amorphous alloys evolve, what microstructures of the alloys transform, and how mechanical and electrochemical behaviors perform through the crystallization processes, the as-spun amorphous alloys were annealed in Ar atmosphere at their specific temperatures, such as the first and second onset and end crystallization temperatures for 15 min. The crystalline structures and phases of these post-annealed samples were analyzed by XRD. Micro hardness was measured on the cross-section of the as-spun and post-annealed samples 10 times with 0.98 N load and 10 s holding time using a FM-700 digital micro hardness tester. The average values with mathematical errors were used as the final results. A Solartron electrochemical interface (Solartron Model SI 1286 and Model SI 1255) was employed to perform potentiodynamic polarization and impedance measurements in 3.56 wt% (0.6 M) NaCl aqueous solution, where the specimen was used as the working electrode, a saturated calomel electrode (SCE) as the reference and a Pt mesh as the counter electrode. All electrode potentials were corrected with ohmic drop and referred to the standard Saturated Calomel Electrode (SCE) scale. Seven typical parameters were chosen to characterize corrosion behavior, i.e. corrosion potential (E_{corr}, or open-circuit potential, OCP), corrosion current density (I_{corr}), passive current density (I_{pass}), pitting potential (E_{pit}), pitting current density (I_{pit}), repassivation potential (E_{rep}), and pitting susceptible region ($\Delta E=E_{pit}-E_{rep}$) determined by potentiodynamic polarization. The electrochemical measurements for each of the alloys were repeated five times, and the average values were utilized as the final results with the uncertainty estimates determined by the least square method.

Results and Analysis

Figure 1 presents the XRD diffraction patterns of the as-spun $Al_{86}Ce_{10}TM_4$ (TM= Fe, Co, Ni and Cu) alloys. Evidently, all the curves exhibit only a main symmetrical broad peak at 2θ between 30 and 45° without any sharp crystalline Bragg peaks in the scanning range between 20 and 80°, manifesting all the as-spun alloys were completely amorphous. The full-amorphous features have also been verified by the TEM examination as shown in Figure 2, where mark A represents the textural micrographs of the as-spun ribbons and mark B represents the diffraction patterns of the texture.

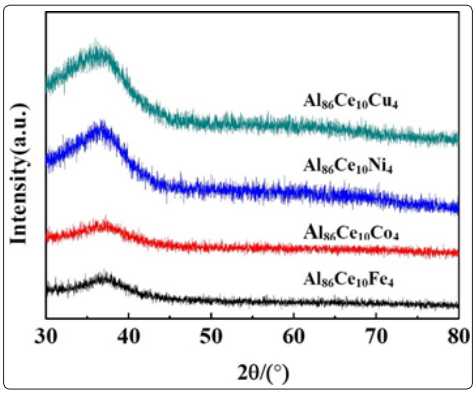

Figure 1: XRD patterns of the as-spun $Al_{86}Ce_{10}TM_4$ (TM=Fe, Co, Ni and Cu) alloys

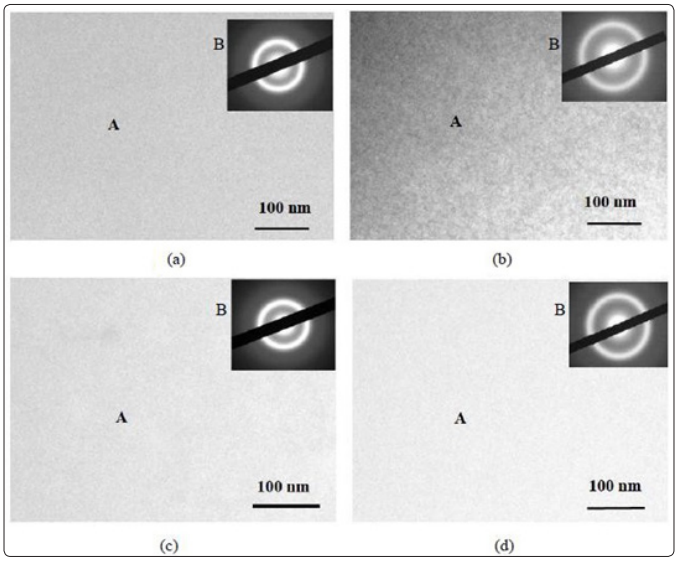

Figure 2: TEM micrographs of the as-spun $Al_{86}Ce_{10}TM_4$ (TM=Fe, Co, Ni and Cu) alloys

To inspect the glass transition and crystallization processes, DSC behavior was investigated by heating the as-spun ribbons from room temperature to 1200 K at heating rates of 20, 40, 80 and 200 K/min as displayed in Figure 3. Obviously, at least two typical crystallization processes were observed from the DSC curves. Such behavior indicates that the final crystallization structures should

have experienced transformations at least through two crystallization steps. Table 1 summarizes the measured parameters, including the glass transition temperature T_g, the onset crystallization temperature T_x, and the crystallization peak temperature T_p. From Figure 3, The apparent crystallization activation energy E and the overall crystallization reaction rate K_0 for each of the two crystallization processes can be determined using Kissinger equation (1) [27-30].

$$\ln\frac{T^2}{\emptyset} = \frac{E}{RT} + C = \frac{E}{RT} + \ln\frac{E}{RK_0}, \qquad (1)$$

Where Ø is the heating rate, R the ideal gas constant. T is a special temperature such as the first and second exothermic peak temperatures T_{p1} and T_{p2}, respectively. C is a constant and K_0 also named as the frequency factor in the Arrhenius law. The relationship of $\ln(T^2/\emptyset)$ versus 1000/T for metallic glasses exhibits an approximate straight line from the Equation (1), thus the parametric values of E and K_0 can be determined from the slope and intercept of the line.

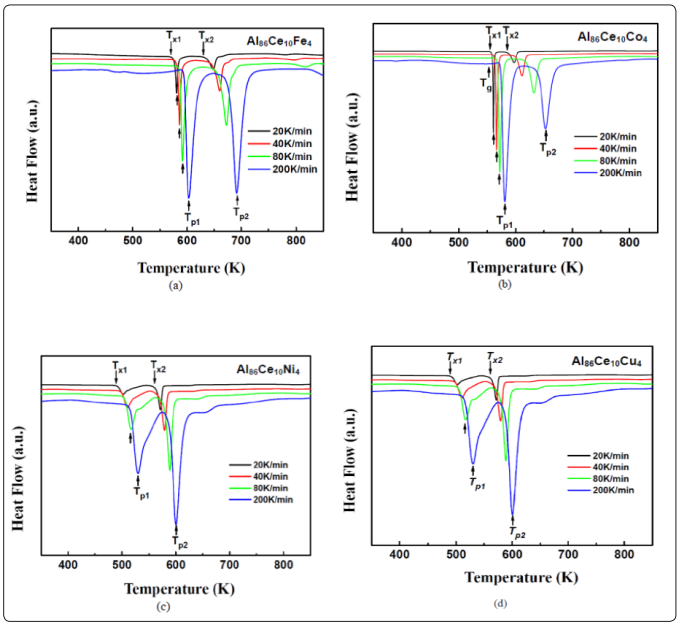

Figure 3: DSC curves of as-spun $Al_{86}Ce_{10}TM_4$ (TM=Fe, Co, Ni and Cu) alloys at heating rates of 20, 40, 80 and 200 K/min, respectively

Table 1: Thermal Parameters of Amorphous $Al_{86}Ce_{10}TM_4$ (TM=Fe, Co, Ni and Cu) Alloys

Sample	Heating Rate (K / min)	T_g (K)	T_{x1} (K)	T_{p1} (K)	T_{x2} (K)	T_{p2} (K)
$Al_{86}Ce_{10}Fe_4$	20	578	578	581	637	648
	40	583	583	586	649	660
	80	588	588	592	660	672
	200	584	595	603	679	692
$Al_{86}Ce_{10}Co_4$	20	560	560	561	588	597
	40	565	565	567	602	611
	80	560	569	572	621	632
	200	568	575	581	641	653
$Al_{86}Ce_{10}Ni_4$	20	522	530	533	610	616
	40	528	535	538	613	618
	80	533	539	543	564	572
	200	539	546	553	583	594
$Al_{86}Ce_{10}Cu_4$	20	493	495	502	564	572
	40	500	500	510	570	579
	80	506	506	517	580	589
	200	517	517	530	589	600

Note: T_g, T_x and T_p represent the glass transition temperature, onset crystallization temperature and peak temperature, respectively determined at heating rates of 20, 40, 80 and 200 K/min. The average standard error is 1 K.

On the other hand, the crystallization kinetic reaction order, n, also called the Avrami exponent can be determined by the Johnson-Mehl-Avrami (JMA) equation (2) [28-32].

$$Ln[-Ln(1-x)]=nLn(k)+nLn(t), \quad (2)$$

Where k is an effective rate constant, n Avrami exponent, x is the crystallized volume fraction in time t.

Figure 4 presents the Kissinger plots of Ln ($T_p^2/Ø$) vs. $1000/T_p$ of the as-spun $Al_{86}Ce_{10}TM_4$ (TM=Fe, Co, Ni and Cu) alloys from which the activation energy E and the frequency factor K_0 are determined. Figure 5 depicts the JMA plots of Ln[-Ln(1-x)] vs. Ln(t) in that the crystallization reaction order n, the Avrami exponent on the first and second exothermic peaks can be quantified. The values of *E*, *Ko* and n as deduced from the slope and intercept of the straight lines from Figures 4 and 5 are tabulated in Table 2.

Based on the onset and end crystallization temperatures as determined from Figure 3 and exhibited in Table 1, annealing of the as-spun fully-amorphous $Al_{86}Ce_{10}TM_4$ (TM=Fe, Co, Ni and Cu) alloys was conducted at these temperatures to investigate what precipitate phases and crystalline structures are and how the precipitate phases evolve. Therefore, the amorphous alloys were annealed each at the onset crystallization and end crystallization temperatures and Figure 6 displays the XRD patterns of the as-spun and post-annealed samples.

In order to further investigate how precipitated crystalline phases influence the mechanical and electrochemical properties, micro-hardness tests and potentiodynamic polarization were carried out on the as-spun and post-annealed samples. For comparison between the as-spun amorphous alloys and the post-annealed alloys with pure Al as reference, Figure 7 shows the potentiodynamic polarization curves of pure Al and as-spun amorphous samples and Figure 8 presents the polarization of the post-annealed samples in the 0.6 M (3.56 wt.%) NaCl aqueous solution. Figure 9 depicts the SEM micrographs on the surface of the post-annealed samples after potentiodynamic polarization test. The measured mechanical hardness and calculated electrochemical parameters are summarized in Table 3.

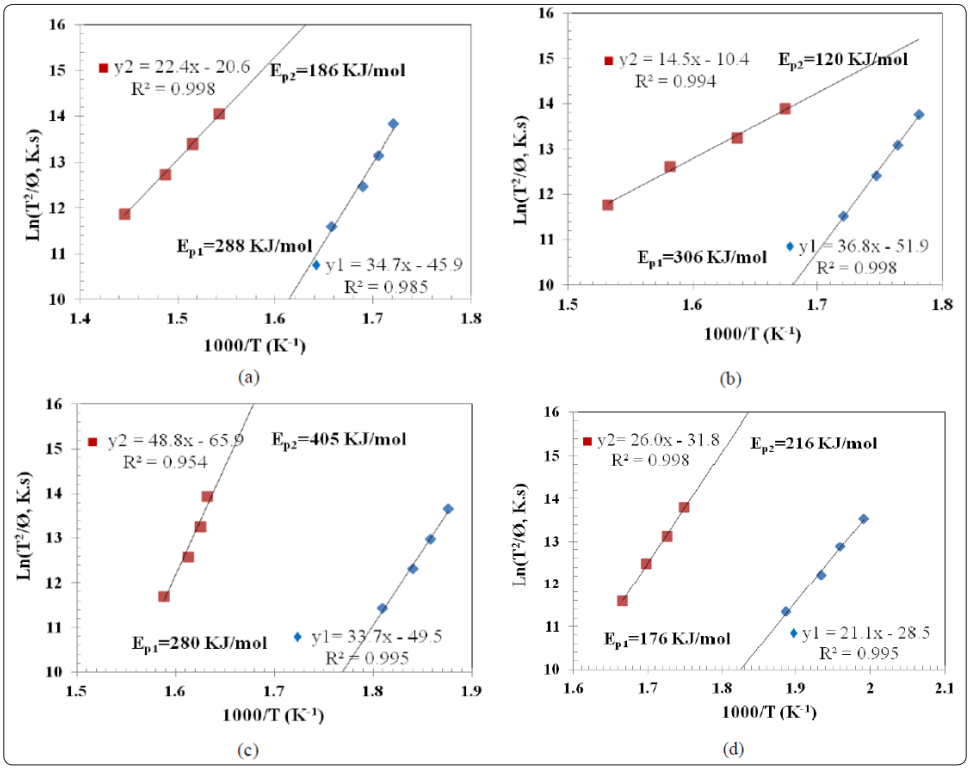

Figure 4: Kissinger plots of Ln ($T_p^2/Ø$) vs. $1000/T_p$ for the crystallization activation energy (E) and frequency factor (K_o) on the first and second exothermic peaks in DSC traces for the as-spun $Al_{86}Ce_{10}TM_4$ (TM=Fe, Co, Ni and Cu) alloys

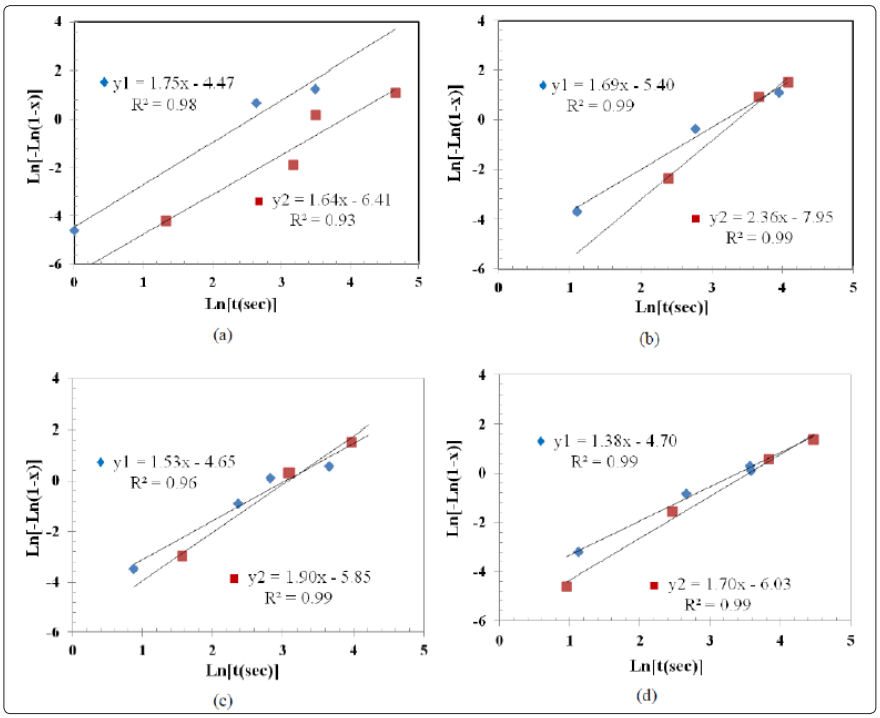

Figure 5: Johnson-Mehl-Avrami (JMA) plots of Ln [-Ln (1-x)] vs. Ln (t) for the Avrami exponent (n) on the first and second exothermic peaks in DSC traces for the as-spun $Al_{86}Ce_{10}TM_6$ (TM=Fe, Co, Ni and Cu) alloys

Table 2: Calculated Values on the First and Second Crystallization Peaks in the Isochronal Scanning DSC Traces for the as-spun $Al_{86}Ce_{10}TM_4$ (TM=Fe, Co, Ni and Cu) Alloys

Alloys	K_{01} (s^{-1})	E_{c1} (KJ/mol)	n_1	K_{02} (s^{-1})	E_{c2} (KJ/mol)	n_2
$Al_{86}Ce_{10}Fe_4$	$3.1*10^{24} \pm 4.1*10^{2}$	288 ± 25	1.75 ± 0.05	$1.9*10^{13} \pm 2.0*10^{3}$	186 ± 22	1.64 ± 0.06
$Al_{86}Ce_{10}Co_4$	$1.3*10^{27} \pm 3.9*10^{3}$	306 ± 11	1.69 ± 0.08	$4.8*10^{8} \pm 5.6*10^{3}$	120 ± 15	2.36 ± 0.04
$Al_{86}Ce_{10}Ni_4$	$1.1*10^{26} \pm 1.6*10^{3}$	280 ± 14	1.53 ± 0.06	$2.0*10^{32} \pm 3.4*10^{3}$	405 ± 35	1.90 ± 0.08
$Al_{86}Ce_{10}Cu_4$	$5.1*10_{16} \pm 2.7*10^{3}$	176 ± 9	1.38 ± 0.05	$2.1*10^{18} \pm 4.5*10^{3}$	216 ± 12	1.40 ± 0.07

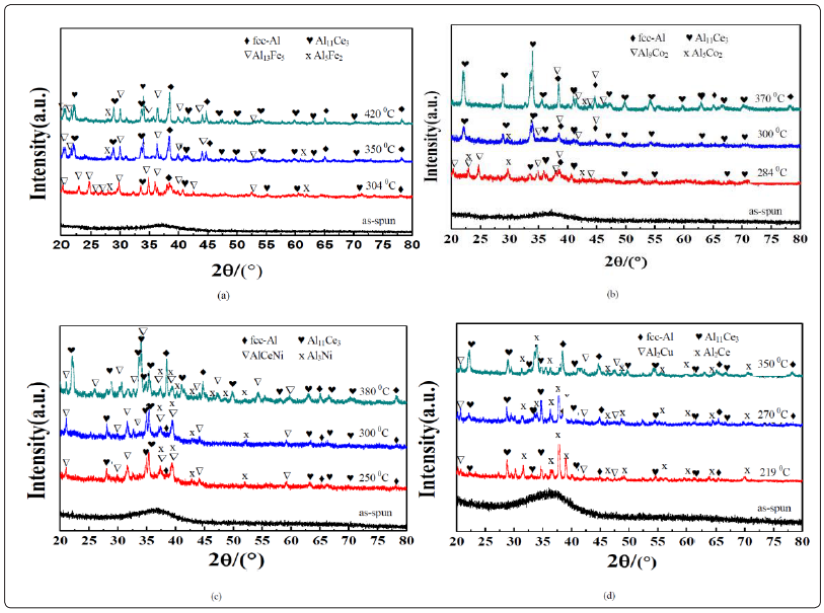

Figure 6: XRD patterns of the as-spun and post-annealed (a) $Al_{86}Ce_{10}Fe_4$ at 304, 350, and 420°C; (b) $Al_{86}Ce_{10}Co_4$ at 284, 300 and 370°C; (c) $Al_{86}Ce_{10}Ni_4$ at 250, 300, and 380°C; and (d) $Al_{86}Ce_{10}Cu_4$ at 219, 270, and 350°C

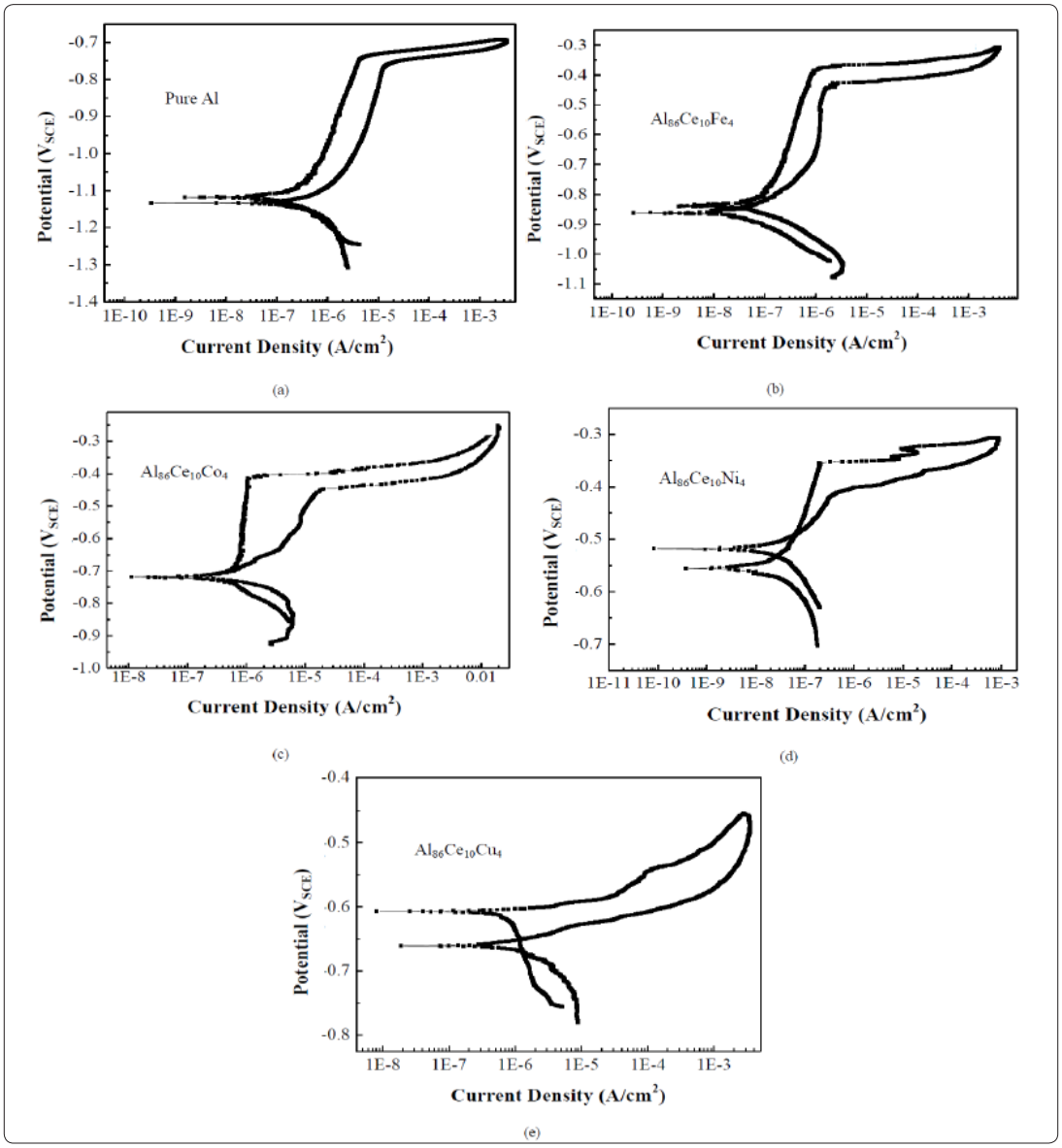

Figure 7: Electrochemical polarization curves of pure Al and the as-spun $Al_{86}Ce_{10}TM_4$ (TM=Fe, Co, Ni and Cu) alloys in 3.56 wt. % NaCl solution

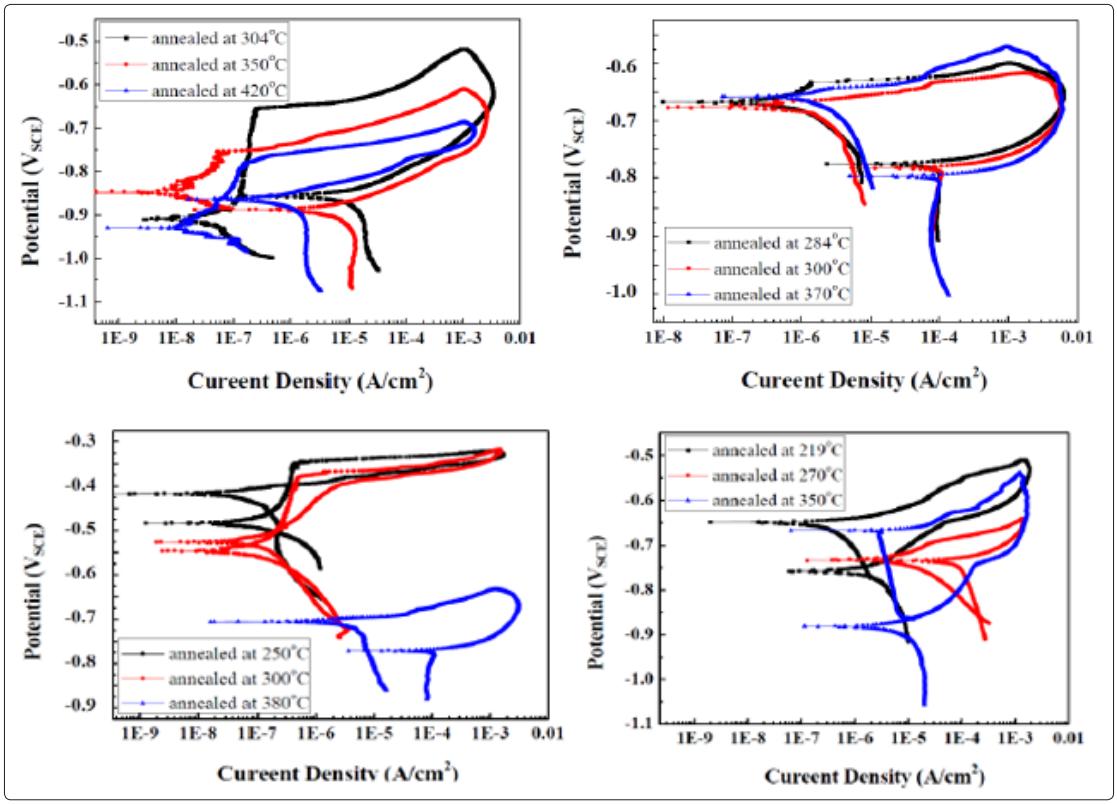

Figure 8: Electrochemical polarization curves of the post-annealed $Al_{86}Ce_{10}TM_4$ (TM=Fe, Co, Ni and Cu) alloys in 3.56 wt. % NaCl solution

Table 3: Electrochemical Data Obtained from Potentiodynamic Polarization in 3.56 wt.% (0.6M) NaCI Aqueous Solution and the Hardness of the as-spun and post-annealed $Al_{86}Ce_{10}TM_4$ (TM=Fe, Co, Ni and Cu) Alloys

Sample	T (°C)	E_{corr} (V_{SCE})	I_{corr} (μA/cm²)	I_{pass} (μA/cm²)	E_{pit} (V_{SCE})	I_{pit} (μA/cm²)	E_{rep} (V_{SCE})	Δ E_{rep} (V_{SCE})	H_v (MPa)
Pure A1	25	-1.10±0.04	0.4±0.2	1.5±0.3	-0.74±0.01	3.9±0.3	-1.14±0.01	0.40±0.01	-
$Al_{86}Ce_{10}Fe_4$	25	-0.87±0.01	0.081±0.004	0.64±0.05	-0.38±0.01	1.0±0.2	-0.45±0.01	0.07±0.02	863±17
	304	-0.91±0.02	0.03±0.01	0.02±0.01	-0.66±0.02	0.20±0.02	-0.86±0.02	0.20±0.02	1165±20
	350	-0.85±0.02	0.02±0.01	0.03±0.02	-0.75±0.02	0.04±0.01	-0.88±0.01	0.13±0.03	984±16
	420	-0.93±0.01	0.02±0.01	0.08±0.02	-0.77±0.01	0.20±0.02	-0.86±0.02	0.09±0.03	1033±18
$Al_{86}Ce_{10}C_{o4}$	25	-0.71±0.00	0.8±0.2	1.0±0.2	-0.44±0.02	1.0±0.2	-0.45±0.01	0.01±0.03	762±20
	284	-0.67±0.03	0.3±0.1	1.0±0.2	-0.63±0.02	1.0±0.2	-0.78±0.02	0.15±0.04	1186±18
	300	-0.68±0.02	0.6±0.2	10±2	-0.63±0.02	60±8	-0.78±0.02	0.15±0.02	1167±16
	370	-0.66±0.03	1.0±0.2	10±2	-0.63±0.02	60±10	-0.80±0.02	0.17±0.04	1053±15
$Al_{86}Ce_{10}Ni_4$	25	-0.54±0.02	0.10±0.08	0.8±0.3	-0.38±0.02	0.5±0.2	-0.43±0.02	0.05±0.04	809±16
	250	-0.46±0.02	0.08±0.02	0.3±0.1	-0.35±0.02	0.4±0.1	-0.50±0.02	0.15±0.04	1066±22
	300	-0.55±0.03	0.05±0.02	0.3±0.2	-0.38±0.02	0.4±0.2	-0.50±0.02	0.12±0.04	912±16
	380	-0.71±0.02	3.0±0.6	-	-	-	-	-	840±18
$Al_{86}Ce_{10}Cu_4$	25	-0.62±0.01	1.0±0.2	20±8	-0.54±0.04	80±10	-0.65±0.03	0.11±0.07	715±11
	219	-0.65±0.02	0.2±0.1	10±2	-0.55±0.02	50±8	-0.75±0.02	0.2±0.04	1020±18
	270	-0.73±0.02	4.0±0.8	20±4	-0.70±0.02	20±5	-0.74±0.02	0.04±0.04	880±15
	350	-0.67±0.03	4.0±1.0	40±12	-0.63±0.03	40±10	-0.89±0.02	0.26±0.04	720±14

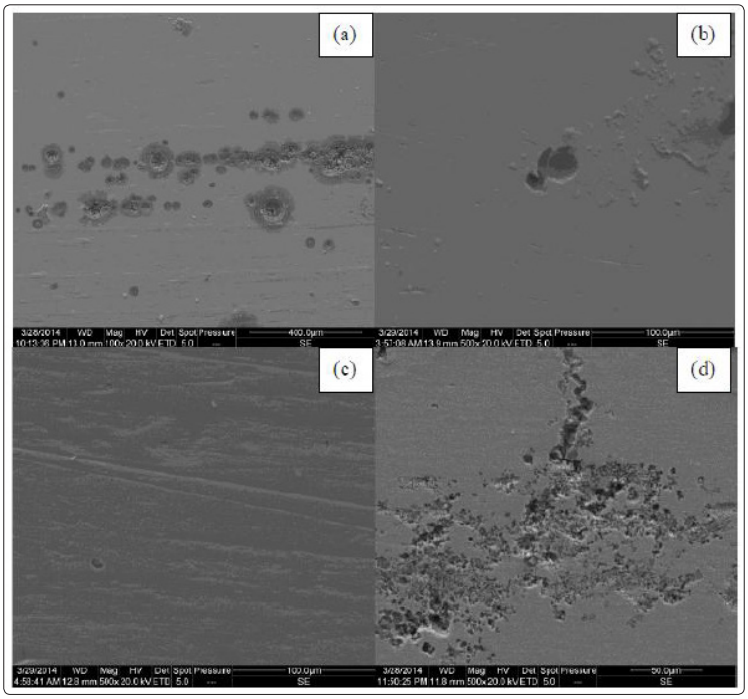

Figure 9: SEM micrographs of the post-annealed $Al_{88}Ce_6TM_6$ (TM: Fe at 304°C (a), Co at 284°C (b), Ni at 250°C (c) and Cu at 219°C (d)) alloys after polarized in 3.56 wt.% NaCl solution

Discussion

The objective of this study is to investigate how the completely amorphous $Al_{86}Ce_{10}TM_4$ (TM=Fe, Co, Ni and Cu) alloys evolve through crystallization processes, what crystalline phases are precipitated, and how the precipitated phases affect the mechanical and corrosion behavior of the alloys.

From Figures 1 and 2, it is identified that the as-spun $Al_{86}Ce_{10}TM_4$ (TM=Fe, Co, Ni and Cu) alloys are completely amorphous without any crystalline phases inside the matrix except a limited amount of short-range-ordered (SRO) Al-TM, Al-Ce and Al-Ce-TM quasi-crystalline clusters are embedded in the matrix, as manifested from our previous paper [25]. Figure 3 elucidates the full-amorphous phase crystallizes through at least two steps with increment of annealing temperature before melting, and the specific temperatures such as T_g, T_x and T_p as measured are tabulated in Table 1. From the analyses of Kissinger's plots as displayed in Figure 4, the activation energies of the amorphous $Al_{86}Ce_{10}TM_4$ (TM=Fe, Co, Ni and Cu) alloys account to 288, 306, 280 and 176 KJ and overall frequencies $3.1x10^{24}$, $1.3x10^{27}$, $1.1x\ 10^{26}$ and $5.1x10^{16}$ s^{-1}, respectively for the first crystallization process, as summarized in Table 2 [27, 30].

The results indicate that the thermal stability of the amorphous alloys ranks in the order of $Al_{86}Ce_{10}Co_4$>$Al_{86}Ce_{10}Ni_4$>$Al_{86}Ce_{10}Fe_4$>$Al_{86}Ce_{10}Cu_4$, which has been demonstrated in our previous report [25]. From the JMA plots in Figure 5, the Avrami exponents are calculated to be 1.75, 1.69, 1.53 and 1.38, respectively on the first crystallization, implying that crystalline nuclei be precipitated predominately in one-dimension, in diffusion controlled manner and from the pre-existing SRO Al-TM, Al-Ce and Al-Ce-TM quasi-crystalline clusters through the crystallization [31,32]. The second crystallization activation energies of the $Al_{86}Ce_{10}TM_4$ (TM=Fe, Co, Ni and Cu) alloys obtained from Figure 4 are 186, 120, 405 and 216 KJ with overall frequencies $1.9x10^{13}$, $4.8x10^{8}$, $2.0x10^{32}$ and $2.1x10^{18}$ s^{-1}, respectively, suggesting the thermal durability of the nanocrystalline nuclei precipitated in the first crystallization process rates as $Al_{86}Ce_{10}Ni_4$>$Al_{86}Ce_{10}Cu_4$>$Al_{86}Ce_{10}Fe_4$>$Al_{86}Ce_{10}Co_4$. The Avrami exponents of the second crystallization from Fig. 5 are calculated to be 1.64, 2.36, 1.90 and 1.40, respectively, indicating that the second crystallization of $Al_{86}Ce_{10}TM_4$ (TM=Fe, Ni and Cu) alloys proceeds preferentially on the pre-precipitated nuclei that grow in one dimension and in diffusion mechanism except $Al_{86}Ce_{10}Co_4$ whose pre-precipitated nuclei grow in two dimensions [31, 32].

What crystalline phases evolve with the crystallization processes? As exhibited in Figure 6 (a), the as-spun completely amorphous $Al_{86}Ce_{10}Fe_4$ alloy starts precipitating nanocrystalline nuclei of (fcc-Al+$Al_{11}Ce_3$+Al_5Fe_2+$Al_{13}Fe_5$) among which the nuclei of $Al_{13}Fe_5$ grow fast at the first onset crystallization temperature 304°C (577K). The precipitated nuclei include fcc-Al (Fm-3m, a=0.405 nm), $Al_{11}Ce_3$ (Immm, a=0.440 nm, b=1.303 nm, c=1.009 nm), Al_5Fe_2 (Cmcm, a=0.766 nm, b=0.642 nm, c=0.422 nm) and $Al_{13}Fe_5$ (C2/m, a=1.549 nm, b=0.808 nm, c=1.247 nm, β=108.03°) [33-38]. All Fe atoms in the alloy are consumed in combining with Al and forming Al_5Fe_2 and $Al_{13}Fe_5$ nanocrystalline precipitates at this temperature due to the limited concentration of Fe (4 at.%) in the alloy. Annealing at 350°C (623K), the first end crystallization temperature, the concentrations of the precipitated crystalline phases Al_5Fe_2 and $Al_{13}Fe_5$ stop increasing but the nuclei of the pre-precipitated crystalline phases fcc-Al and $Al_{11}Ce_3$ grow fast till all Ce atoms are used up for forming the $Al_{11}Ce_3$ crystals. The crystallization process in the first exothermal peak shows 288 KJ in overall crystallization activation energy, $3.1x10^{24}$ in crystallization frequency and 1.75 in Avrami exponent. When annealing temperature rises to the second onset crystallization temperature 420°C (693K), the $Al_{11}Ce_3$, Al_5Fe_2 and $Al_{13}Fe_5$ crystalline phases stop growth due to the exhaust of Ce and Fe in forming these intermetallics in the alloy, but growth of fcc-Al crystalline phases dominates in the second crystallization

process, where crystallization activation energy accounts to 186 KJ, crystallization frequency $1.9x10^{13}$ and Avrami exponent 1.64.

For the completely amorphous $Al_{86}Ce_{10}Co_4$ alloy shown in Figure 6 (b), annealing at the first onset crystallization temperature 284°C (557K) instigates nucleation of (fcc-Al+$Al_{11}Ce_3$+Al_5Co_2+Al_9Co_2) nanocrystalline particles, among which Al_9Co_2 nuclei grow fast till all Co atoms are consumed in forming Al_5Co_2 and Al_9Co_2 phases. The precipitated phases are fcc-Al, $Al_{11}Ce_3$, Al_5Co_2 ($P6_3/mmc$, a=0.767 nm, c=0.761 nm) and Al_9Co_2 ($P2_1/a$, a=0.857 nm, b=0.629 nm, c=0.621 nm, β=94.76°) [33, 37]. Annealing at the first end crystallization temperature 300°C (573K), fcc-Al, Al_5Co_2 and Al_9Co_2 nanocrystalline precipitates cease growing but $Al_{11}Ce_3$ precipitates keep growing. The first crystallization exothermal peak presents 306 KJ in overall crystallization activation energy, $1.3x10^{27}$ in crystallization frequency and 1.69 in Avrami exponent. Further annealing at the second onset crystallization temperature 370°C (643K) makes (fcc-Al+$Al_{11}Ce_3$) nanocrystalline phases grow fast. The second crystallization peak shows overall crystallization activation energy 120 KJ, crystallization frequency $4.8x10^8$ and Avrami exponent 2.36.

Regarding the completely amorphous $Al_{86}Ce_{10}Ni_4$ alloy depicted in Figure 6 (c), (fcc-Al+$Al_{11}Ce_3$+Al_3Ni+AlCeNi) nuclei are precipitated at the first onset crystallization temperature 250°C (523K) in that the AlCeNi nuclei precipitate fast. The precipitated crystalline phases consist of fcc-Al, $Al_{11}Ce_3$, Al_3Ni (Pnma, a=0.661 nm, b=0.739 nm, c=0.481 nm) and AlCeNi (P-62m, a=0.698 nm, c=0.402 nm) [39]. The concentrations of (fcc-Al+$Al_{11}Ce_3$+Al_3Ni+AlCeNi) nanocrystalline precipitates keep constant even if the alloy is annealed at the first end crystallization temperature 300°C (573K). However, when the alloy is annealed at the second onset crystallization temperature 380°C (653K), fast growth of fcc-Al and $Al_{11}Ce_3$ nanocrystalline phases is spurred while growth of Al_3Ni and AlCeNi phases stops because Ni has been exhausted in forming the intermetallics at 250°C (523K). The first crystallization exothermal peak shows overall crystallization activation energy 280 KJ, crystallization frequency $1.1x10^{26}$ and Avrami exponent 1.53. The second crystallization exothermal peak presents overall crystallization activation energy 405 KJ, crystallization frequency $2.0x10^{32}$ and Avrami exponent 1.90.

Considering the completely amorphous $Al_{86}Ce_{10}Cu_4$ alloy displayed in Figure 6 (d), (fcc-Al+$Al_{11}Ce_3$+Al_2Cu+Al_2Ce) nanocrystalline nuclei are precipitated at the first onset crystallization temperature 219°C (492K), among which Al_2Ce nanocrystalline precipitates grow fast. The precipitated nuclei contain fcc-Al, $Al_{11}Ce_3$, Al_2Cu (I4/mcm, a=0.606 nm, c=0.487 nm) and Al_2Ce (Fd-3m, a=0.807) [34-38]. The concentrations of the (fcc-Al+$Al_{11}Ce_3$+Al_2Cu+Al_2Ce) precipitates maintain stabilized at the first end crystallization temperature 270°C (543K). However, growth of fcc-Al and $Al_{11}Ce_3$ nanocrystalline nuclei speeds up while Al_2Cu and Al_2Ce precipitates stop growing at the second onset crystallization temperature 350°C (623K). The first crystallization exothermal peak shows overall crystallization activation energy 176 KJ, crystallization frequency $5.1x10^{16}$ and Avrami exponent 1.38. The second crystallization exothermal peak presents overall crystallization activation energy 216 KJ, crystallization frequency $2.1x10^{18}$ and Avrami exponent 1.40.

To better understand how the nanocrystalline precipitates or the composite structures influence the mechanical and electrochemical properties, micro-hardness test and potentiodynamic polarization were conducted on the as-spun and post-annealed samples. For comparison, Figure 7 shows the electrochemical polarization curves of pure Al and the as-spun full amorphous $Al_{86}Ce_{10}TM_4$ (TM=Fe, Co, Ni and Cu) alloys while Figure 8 presents the polarization of the post-annealed $Al_{86}Ce_{10}TM_4$ (TM=Fe, Co, Ni and Cu) alloys in 0.6 M NaCl aqueous solution. The electrochemical and mechanical data are provided in Table 3.

It can be interestingly found that the completely amorphous $Al_{86}Ce_{10}TM_4$ (TM=Fe, Co, Ni and Cu) alloys exhibit mechanical hardness 863, 762, 809 and 712 MPa, respectively, higher than those of the traditional Al crystalline alloys such as AA 2024, AA 6061 and AA 7075 which normally present hardness 500-600 MPa. This is because $Al_{86}Ce_{10}TM_4$ (TM=Fe, Co, Ni and Cu) alloys consist of amorphous matrix embedded with a tiny amount of short-range ordered (SRO) quasi-crystalline clusters, where the amorphous state of disordered atomic packing introduces lot of stress and strain that strengthen the amorphous matrix. In addition, the solute (Ce and TM atoms) enrichment and SRO quasi-crystalline clusters enhance the matrix in mechanisms of solute strengthening and precipitation hardening [25].

After the as-spun $Al_{86}Ce_{10}TM_4$ (TM=Fe, Co, Ni and Cu) alloys are annealed at the first onset crystallization temperatures 304 (577K), 284 (557K), 250 (523K) and 219 (492K) °C, respectively for 15 min, nanocrystalline nuclei are precipitated from the amorphous matrix, in which small volume of fcc-Al, $Al_{11}Ce_3$, $Al_{13}Fe_5$, and Al_5Fe_2 nanocrystals in size of 5~23 nm are embedded in amorphous matrix of $Al_{86}Ce_{10}Fe_4$; fcc-Al, $Al_{11}Ce_3$, Al_5Co_2, and Al_9Co_2 nanocrystals in size of 8~20 nm in amorphous $Al_{86}Ce_{10}Co_4$; fcc-Al, $Al_{11}Ce_3$, AlCeNi and Al_3Ni nanocrystals in size of 14~20 nm in amorphous $Al_{86}Ce_{10}Ni_4$; and fcc-Al, $Al_{11}Ce_3$, Al_2Ce and Al_2Cu nanocrystals in size of 11~15 nm in amorphous $Al_{86}Ce_{10}Cu_4$ (where the size of the precipitates was determined from $D=2\pi/\Delta Q$, where ΔQ is the full width at half maximum (FWHN) of the XRD peaks [25]). In this case, the mechanical hardness increases compared to the completely amorphous matrix because of the precipitate hardening effect of the nano-sized crystals in the amorphous matrix.

Annealing at the first end crystallization temperature may result in further increment in volume of crystalline phases and in size of the crystalline particles, in particular more concentrations of fcc-Al and $Al_{11}Ce_3$ nanocrystals in size of 13~23 nm with Al_5Fe_2 and $Al_{13}Fe_5$ intermetallic particles in size of 15~23 nm are present in $Al_{86}Ce_{10}Fe_4$; constant volume of fcc-Al, $Al_{11}Ce_3$, Al_5Co_2 and Al_9Co_2 nanocrystals in size of 8~20 nm are maintained in $Al_{86}Ce_{10}Co_4$; minor increasing volume of fcc-Al, $Al_{11}Ce_3$, Al_3Ni and AlCeNi nanocrystals in size of 10~33 nm are grown in $Al_{86}Ce_{10}Ni_4$; and slightly increasing volume of fcc-Al, $Al_{11}Ce_3$, Al_2Cu and Al_2Ce nanocrystals in size of 11~15 nm are deposited in $Al_{86}Ce_{10}Cu_4$. In this case, mechanical hardness may continuously increase, or keep unchanged, or slightly decrease if amorphous alloys are annealed at the first end crystallization temperature depending upon the overall precipitate volume, precipitate distribution, precipitate composition and precipitate sizes in the amorphous matrix, which either enhance, maintain or weaken mechanical hardness of the alloys. The hardness of the alloys lies on the volume, the size, the composition and the distribution of the crystalline precipitates in the amorphous matrix.

Annealing at higher temperature, such as the second onset or end crystallization temperature drives continuous growth of the crystalline precipitates and further devitrification of the alloys. Therefore, fcc-Al, $Al_{11}Ce_3$, $Al_{13}Fe_5$ and Al_5Fe_2 crystals in size of 12~24 nm are found in $Al_{86}Ce_{10}Fe_4$; fcc-Al, $Al_{11}Ce_3$, Al_9Co_2 and Al_5Co_2 crystals in size of 23~31 nm are presented in $Al_{88}Ce_8Co_4$; fcc-Al, $Al_{11}Ce_3$, AlCeNi and Al_3Ni precipitates in size of 15~33 nm are observed in $Al_{86}Ce_{10}Ni_4$; and fcc-Al, $Al_{11}Ce_3$, Al_2Ce and Al_2Cu precipitates in size of 10~29 nm are formed in $Al_{86}Ce_{10}Cu_4$ as analyzed from Figure 6. Since annealing may pass over the ideal point where the alloys present the maximum mechanical hardness with the best optimized amorphous-crystalline mixed structure, thus mechanical hardness starts dropping with annealing at higher temperature and for longer duration till the full amorphous matrix initially converts to amorphous-crystalline mixed structure at the first onset crystallization temperature, and finally transforms into completely polycrystalline phases at the second end crystallization temperature, which present the same structure as the traditional Al polycrystalline alloys.

To check how electrochemical properties evolve with crystallization processes, polarization techniques were applied to the as-spun and post-annealed alloys as exhibited in Figures 7 and 8. Compared to pure Al, the as-spun full amorphous $Al_{86}Ce_{10}TM_4$ (TM=Fe, Co, Ni and Cu) alloys exhibit better corrosion resistance except $Al_{86}Ce_{10}Cu_4$, demonstrating the superior corrosion resistance of the amorphous alloys in comparison to their crystalline counterparts except a few cases where the high susceptibility to corrosion ascribes to the nature of the alloy itself such as $Al_{86}Ce_{10}Cu_4$ [25].

Interestingly, like the same evolution sequence in mechanical behavior, annealing at the first onset crystallization temperature confers the alloys higher corrosion resistance as well. This should be attributed to the amorphous phase embedded with tiny nanocrystalline nuclei where there appears no distinct difference in electrochemical potential between the amorphous matrix and precipitated nanocrystalline phases. Consequently, the composite structure confers equivalent or even superior corrosion resistance compared to the full amorphous structure, as displayed for the as-spun $Al_{86}Ce_{10}TM_4$ (TM=Fe, Co, Ni and Cu) alloys after annealed at the first onset and end crystallization temperatures shown in Figure 8 and Table 3.

However, annealing at higher temperature causes severe devitrification of the amorphous texture, thus generating higher volume crystalline particles in larger sizes. These crystalline phases present sufficient electrochemical difference from the amorphous matrix, thus nano-electrochemical cell between the precipitated crystalline particles and the amorphous matrix surrounding the crystals triggers the matrix high susceptible to corrosion [40-43]. This phenomena can be evidently observed on the $Al_{86}Ce_{10}TM_4$ (TM=Fe, Co, Ni and Cu) alloys after annealed at the second onset crystallization temperature. Even worse corrosion resistance can be anticipated if the samples be annealed at higher temperature such as the second end crystallization temperature or for longer time, because the alloys would be transforming to completely polycrystalline structures with larger-sized crystalline particles, between which the electrochemical cell in large potential difference takes in effect. As a result, the corrosion susceptibility depends on how much crystallization evolves so that how large electrochemical potentials differ between the precipitated crystalline phases or/and the Al matrix in environment. From the electrochemical polarization results, the post-annealed $Al_{86}Ce_{10}TM_4$ (TM=Fe, Co, Ni and Cu) alloys exhibit the electrochemical corrosion resistance as $Al_{86}Ce_{10}Fe_4$>$Al_{86}Ce_{10}Ni_4$>$Al_{86}Ce_{10}Co_4$> $Al_{86}Ce_{10}Cu_4$ because $Al_{86}Ce_{10}Fe_4$ alloy even after annealed at 402°C (675K) for 15 min still exhibits the best resistance to corrosion. The corrosion resistant rate and high temperature durability can list the alloys in sequence of $Al_{86}Ce_{10}Fe_4$ 402°C>$Al_{86}Ce_{10}Ni_4$ 300°C>$Al_{86}Ce_{10}Co_4$ 284°C>$Al_{86}Ce_{10}Cu_4$ 219°C, as interpreted from Figure 8 and Table 3.

Figure 9 shows the SEM micrographs on the surface of the post-annealed $Al_{86}Ce_{10}TM_4$ (TM=Fe, Co, Ni and Cu) alloys at the first onset crystallization temperatures, 304 (577K), 284 (557K), 250 (523K) and 219 (492K) °C for 15 min, respectively after they were polarized in 0.6 M NaCl solution. As seen from Figure 9, the post-annealed $Al_{86}Ce_{10}Cu_4$ at 219°C (492K) after polarization exhibits the worst corrosion resistance because high density and large area of corrosion pits are visualized. The post-annealed $Al_{86}Ce_{10}Fe_4$ at 304°C (577K) after polarization shows the second least corrosion resistance where visible pits are present on the surface. The post-annealed $Al_{86}Ce_{10}Ni_4$ at 250°C (523K) and $Al_{86}Ce_{10}Co_4$ at 284°C (557K) shows excellent corrosion resistance where no or limited pits are observed after polarization. Such pits as seen on the samples should be ascribed to the precipitated intermetallic crystalline particles, the $Al_{11}Ce_3$, Al_5Fe_2 and $Al_{13}Fe_5$ nanocrystals in $Al_{88}Ce_{10}Fe_4$; the $Al_{11}Ce_3$, Al_5Co_2 and Al_9Co_2 in $Al_{86}Ce_{10}Co_4$; the $Al_{11}Ce_3$, Al_3Ni and AlCeNi in $Al_{86}Ce_{10}Ni_4$; and the $Al_{11}Ce_3$, Al_2Cu and Al_2Ce in $Al_{86}Ce_{10}Cu_4$; normally possess more noble electrochemical potentials than the Al phase (either amorphous Al matrix or fcc-Al crystals) [25, 41-43].

As a result, the intermetallic precipitates and their surrounded Al phase set up nano-electrochemical cell where the former acts as the cathode while the later plays as the anode. The Al phase around the intermetallic precipitates is preferentially corroded so that the intermetallic particles are eventually stripped off after the surrounding Al phase is completely corroded away. The sizes of the pits should be larger than those of the precipitated intermetallic particles, in this case, pits over 20~40 nm are usually visualized in the Figure 9. From Figure 9 the corrosion resistance can list as $Al_{86}Ce_{10}Ni_4$>$Al_{86}Ce_{10}Co_4$>$Al_{86}Ce_{10}Fe_4$>$Al_{86}Ce_{10}Cu_4$. This observation looks a little different from the electrochemical polarization results as shown in Figure 8 and Table 3 where $Al_{86}Ce_{10}Fe_4$ was listed as the best corrosion resistant. The difference should be attributed to the higher annealing temperature, 304°C (577K) for $Al_{86}Ce_{10}Fe_4$ than 284°C (557K) for $Al_{86}Ce_{10}Ni_4$ and 250°C (523K) for $Al_{86}Ce_{10}Co_4$ that more volume of nanocrystalline particles in larger sizes are precipitated in $Al_{86}Ce_{10}Fe_4$ thus higher susceptibility to corrosion as observed from Figure 9.

Conclusions

Completely amorphous $Al_{86}Ce_{10}TM_4$ (TM=Fe, Co, Ni and Cu) alloys were fabricated by fast-quenching technique. The crystallization evolution was investigated by DSC and XRD techniques. Mechanical and electrochemical behavior was studied by micro-hardness and potentiodynamic polarization techniques. The crystallization of the amorphous $Al_{86}Ce_{10}TM_4$ (TM=Fe, Co, Ni and Cu) alloys exhibit two exothermal processes, where the first exothermal peak represents nucleation of nanocrystalline phases from the amorphous matrix while the second exothermal peak shows the growth of the precipitated nuclei. It is important to note that

annealing at temperature lower than the second end crystallization temperature in most, but preferentially in the range between the first and second onset temperatures, plays an essential rule on fabricating an ideal amorphous nanocrystalline mixed structure that confers not only optimized mechanical hardness but also best corrosion resistance. It is important to note that fabricating such ideal amorphous-nanocrystalline mixed structure for the $Al_{86}Ce_{10}TM_4$ (TM= Fe, Co, Ni and Cu) alloys can provide substantially improved mechanical hardness (2 times), corrosion resistance (10 times) and high temperature durability (350°C) compared to the traditional Al crystalline alloys, and thus make potential breakthrough on both scientific investigation and engineering application.

Acknowledgements

This work was supported by National Natural Science Foundation of China under the grants of NNSF Nos. 50642034, 20963006, 51061012, 51161014 and 51761035; the Ministry of Science and Technology of China under the grant No. of 2012DFA51260; and the Inner Mongolia Key Natural Science Foundation of China under the grant No. of 2017ZD03. The authors gratefully acknowledge the above financial supports.

References

1. A Inoue (1998) Amorphous, nanoquasicrystalline and nanocrystalline alloys in Al-based systems. Progress in Material Science 43: 365-520.
2. WL Johnson (1988) Crystal-to-glass transformation in metallic materials. Mater. Sci. Eng 97: 1-13.
3. WH Wang, C Dong, CH Shek (2004) Bulk Metallic Glasses. Mater Sci. Eng. R 44: 45-98.
4. Y He, SJ Poon, GJ Shiflet (1988) Synthesis and Properties of Metallic Glasses That Contain Aluminum. Science 241: 1640-1642.
5. A Inoue, K Ohtera, AP Tsai, T Masumoto (1988) New Amorphous Al-Y, Al-La and Al-Ce Alloys Prepared by Melt Spinning. Jpn. J. Appl. Phys 27.
6. DE Polk (1972) The structure of glassy metallic alloys Structure des alliages metalliques vitreux Die struktur glasähnlicher metallischer Legierungen. Acta Metall 20: 485-491.
7. SR Nagel, J Tauc (1975) Nearly-Free-Electron Approach to the Theory of Metallic Glass Alloys. Phys. Rev. Lett 35: 380-383.
8. SH Whang (1983) New prediction of glass-forming ability in binary alloys using a temperature-composition map. Mater. Sci. Eng 57: 87-95.
9. PK Singh, KS Dubey (2010) Analysis of Thermodynamic Behavior of Bulk Metallic Glass Forming Melts and Glass Forming Ability. J. Therm. Anal. Calorim 100: 347-353.
10. A Inoue, K Ohtera, AP Tsai, HM Kimura, T Masumoto (1988) New Amorphous Al-Y, Al-La and Al-Ce Alloys Prepared by Melt Spinning. Jpn. J. Appl. Phys 27: L1579-L1584.
11. M Hagiwara, A Inoue, HH Lieberman (Ed.) (1993) Rapidly Solidified Alloys, Marcel Dekker, New York.
12. M Malekan, SG Shabestari, R Gholamipour, SH Seyedein (2009) Effect of Ge addition on mechanical properties and fracture behavior of Cu–Zr–Al bulk metallic glass. J. Alloys Compd 484: 708-711.
13. M Salehi, SG Shabestari, SMA Boutorabi (2013) Mater. Sci. Eng. A 586: 407-412.
14. JE Sweitzer, GJ Shiflet, JR Scully (2003) Localized corrosion of Al90Fe5Gd5 and Al87Ni8.7Y4.3 alloys in the amorphous, nanocrystalline and crystalline states: Resistance to micrometer-scale pit formation. Electrochim. Acta 48: 1223-1234.
15. AM Lucente, JR Scully (2007) Pitting and alkaline dissolution of an amorphous–nanocrystalline alloy with solute-lean nanocrystals. Corros. Sci 49: 2351-2361.
16. GH Li, WM Wang, HJ Ma, R Li, ZH Zhang, et al. (2011) Effect of different annealing atmospheres on crystallization and corrosion resistance of $Al_{86}Ni_9La_5$ amorphous alloy. Mater. Chem. Phys 125: 136-142.
17. F Ye, K Lu, J (2000) Crystallization kinetics of Al-La-Ni amorphous alloy. Non-Cryst. Solids 262: 228-235.
18. P Gargarella, CS Kiminami, MF de Oliveira, C Bolfarini, WJ Botta (2010) Crystallisation behaviour and glass-forming ability in Al–La–Ni system. J. Alloys Compd. 495: 334-337.
19. JQ Wang, YH Liu, S Imhoff, N Chen, DV Louzguine-Luzgin, et al. (2012) Enhance the thermal stability and glass forming ability of Al-based metallic glass by Ca minor-alloying. Intermetallics 29: 35-40.
20. X Hu, J Guo, G Fan, T Feng (2013) Evaluation of glass-forming ability for Al-based amorphous alloys based on superheated liquid fragility and thermodynamics. J. Alloys Compd. 574: 18-21.
21. T Gloriant, AL Greer (1998) Al-based nanocrystalline composites by rapid solidification of Al-Ni-Sm alloys. NanoStrudured Mater 10: 389-396.
22. TV Kulikova, VA Bykov, AA Belozerova, AM Murzakaev, RE Ryltsev (2013) Crystallization kinetics of Al86Ni8Gd6 amorphous alloy. J. Non-Cryst. Solids 378: 135-138.
23. SA Uporov, NS Uporova, VA Bykov, TV Kulikova, SV Pryanichnikov (2014) Effect of replacing RE and TM on magnetic properties and thermal stability of some Al–Ni-based amorphous alloys. J. Alloys Compd. 586: S310–S313.
24. Y-H Kim, A Inoue, T Masumoto (1991) Increase in mechanical strength of Al-Y-Ni amorphous alloys by dispersion of nanoscale FCC aluminium by FCC aluminium particles. Mater. Trans. JIM 32: 331-338.
25. J Zhang, P Shi, A Chang, T Zhao, W Li, et al. (2019) Glass-forming ability, thermal stability, mechanical and electrochemical behavior of Al-Ce-TM (TM = Ti, Cr, Mn, Fe, Co, Ni and Cu) amorphous alloys. J. Non-Cryst. Solids X 1: 100005.
26. A Inoue (2000) Stabilization of metallic supercooled liquid and bulk amorphous alloys. Acta Mater 48: 279-306.
27. HE Kissinger (1956) Variation of Peak Temperature With Heating Rate in Differential Thermal Analysis. J. Res. Natl. Bur. Stand 57: 217-221.
28. N Afify (2008) A new method to study the crystallization or chemical reaction kinetics using thermal analysis technique. Journal of Physics and Chemistry of Solids 69: 1691-1697.
29. SH Al-Heniti (2009) Kinetic study of non-isothermal crystallization in Fe78Si9B13 metallic glass. J. Alloys and Compd 484: 177-184.
30. RMR Wellen, EL Canedo (2014) On the Kissinger equation and the estimate of activation energies for non-isothermal cold crystallization of PET. Polymer Testing 40: 33-38.
31. Z Sun, X Wang, F Guo, C Jiang, Q Pan (2016) Isothermal and nonisothermal crystallization kinetics of bio-sourced nylon 69. Chinese Journal of Chemical Engineering 24: 638-645.
32. N Afify (1992) Calorimetric study on the crystallization of a Se0.8Te0.2 chalcogenide glass. J. Non-Cryst. Solids 142: 247-275.

33. L Zhu, S Soto-Medina, RG Hennig, M V Manuel (2019) Experimental investigation of the Al–Co–Fe phase diagram over the whole composition range. J. Alloys and Compd 815: 152110.
34. L Zhu, S Soto-Medina, W Cuadrado-Castillo, RG Hennig, MV Manuel (2019) New experimental studies on the phase diagram of the Al-Cu-Fe quasicrystal-forming system. J. Alloys and Compd 185: 108186.
35. J Su, F Guo, H Cai, L Liu (2019) Structural analysis of Al–Ce compound phase in AZ-Ce cast magnesium alloy. Journal of Materials Research Technology.
36. NA Belov, AV Khvan (2007) The ternary Al–Ce–Cu phase diagram in the aluminum-rich corner. Acta Materialia 55: 5473-5482.
37. Y Sun, C Hung, RJ Hebert, C Fennessy, A Tulyani, et al. (2019) Eutectic Microstructures in Dilute Al-Ce and Al-Co Alloys. Materials Characterization 154: 269-276.
38. V Raghavan (2008) JPEDAV 29: 264-266. DOI: 10.1007/s11669-008-9288-x.
39. C Tang, Y Du, H Zhou (2009) The phase equilibria of the Al–Ce–Ni system at 500 °C. J. Alloys and Compd 470: 222-227.
40. B Zhao, Y Zhan, H Tang (2019) High-temperature properties and microstructural evolution of Al–Cu–Mn-RE (La/Ce) alloy designed through thermodynamic calculation. Materials Science and Engineering A 758: 7-18.
41. N Birbilis, RB Buchheit (2005) Electrochemical Characteristics of Intermetallic Phases in Aluminum Alloys. J Electrochem. Soc 152: B140-B151.
42. NR Tailleart (2012) Effect of thermally induced relaxation on passivity and corrosion of an amorphous Al–Co–Ce alloy. Corrosion Science 59: 238-248.
43. RK Gupta, NL Sukiman, MK Cavanaugh, BRW Hinton, CR Hutchinson, et al. (2012) Metastable pitting characteristics of aluminium alloys measured using current transients during potentiostatic polarization. Electrochimica Acta 66: 245-254.